CrossMark

Investigation on the AC and DC electrical conductivity of $Sn_3Sb_2S_6$ thin films prepared by glancing angle deposition

A. Larbi[1] · I. Trabelsi[1] · H. Dahman[2] · M. Kanzari[1,3]

Abstract

$Sn_3Sb_2S_6$ thin films were deposited by single source vacuum thermal evaporation using glancing angle deposition technique. The incident angle α between the particle flux and the normal to the substrate was varied from 0° to 85°. The structural, morphological and electrical properties were investigated by X-ray diffraction, scanning electron microscopy, and impedance spectroscopy, respectively. The effect of these properties as a function of the incident angle has been studied. The AC conductivity exhibited a Jonscher's universal power law. It is observed that exponent s decreases with increasing measurement temperature. Further analysis revealed that, samples AC conductivity follows the correlated barrier hopping model. The Cole–Cole plot showed a single semicircle, indicating an equivalent circuit with a single parallel resistor R and capacitance C network. The activation energy obtained from both angular relaxation frequency and DC conductivity suggests that the carrier transport mechanism is a hopping mechanism thermally activated in the band gap.

1 Introduction

The ternary semiconductor $Sn_3Sb_2S_6$ appears to be one of the most promising candidates owing to their important properties for film solar cell [1]. Indeed, it has potential for high conversion efficiency due to its high absorption coefficient of approximately 10^5 cm^{-1} and it direct band gap of 1.47–1.18 eV [1], which matches well to the solar spectrum. $Sn_3Sb_2S_6$ has an orthorhombic system with space group Pnma and lattice parameters a = 23.18, b = 3.965, c = 34.94 Å [2]. Considerable efforts have been made to obtain a surface with varying topography on the nanometer length scale for various applications. The deposition at oblique angles is one of the solutions. The oblique angle configuration has emerged as an invaluable tool for the deposition of nanostructured thin films. The last 20–25 years have witnessed the systematic application of oblique angle deposition (OAD) procedures for the development of a large variety of devices in fields such as sensor technology, photovoltaic cells, magnetism, optical devices, electrochemistry and catalysis [3]. This method has been applied to produce films with various microstructures. In this article we chose to prepare the $Sn_3Sb_2S_6$ thin films by thermal evaporation method onto glass/silicon substrates with the glancing angle deposition (GLAD) technique. This paper describes the microstructure and electric properties of $Sn_3Sb_2S_6$ thin films.

2 Experimental details

$Sn_3Sb_2S_6$ crystal has been synthesized by direct reaction of high purity elemental materials of tin, antimony and sulfur. Thin films of $Sn_3Sb_2S_6$ were prepared by thermal evaporation from a molybdenum boat using the GLAD technique at a pressure of 10^{-6} Torr at room temperature. The substrates were placed directly above the source at a distance of 10 cm. The deposition angle α was fixed at 0°, 40°, 60°, 75° and 85°. A schematic drawing of the film deposition system is shown in Fig. 1.

The crystallographic structure of the films was examined by Philips X'Pert X-ray diffractometer using CuKα radiation (λ = 0.154056 nm). The high tension and current were 40 kV and 30 mA. The cross-sectional structure was examined by field emission scanning electron microscopy (Zeiss Ultra 40 microscope). A Hewlett-Packard

✉ H. Dahman
  h_dahman_2000@yahoo.com

1 Laboratoire de Photovoltaïque et Matériaux Semiconducteurs, ENIT-El Manar University, Tunis, Tunisia

2 Laboratory of Physics of Materials and Nanomaterials Applied at Environment (LaPhyMNE), Faculty of Sciences, Gabes University, 6072 Gabès, Tunisia

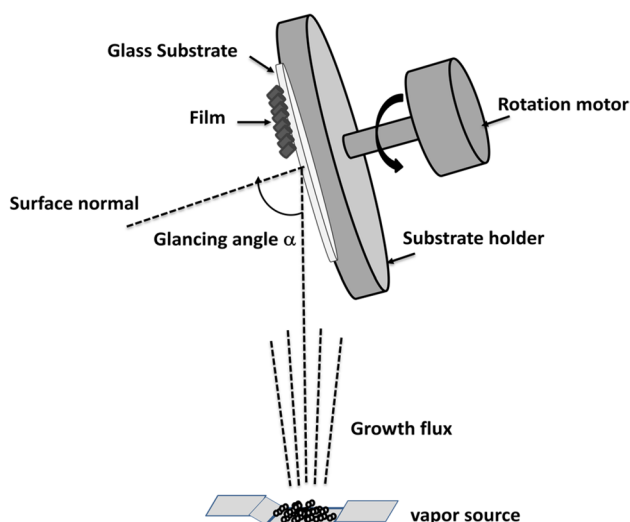3 IPEI Tunis Montfleury-Université de Tunis, Tunis, Tunisia

Fig. 1 Schematic diagram of the GLAD technique

4192 analyzer was used to measure the impedance components (Z′ and Z″) over a wide range of temperatures (420–500 °C); frequencies (1 KHz–13 MHz). Configuration for electrical measurements was performed using two electrodes painted at both ends of the sample, in coplanar mode, using a conductive silver paste as shown in Fig. 2.

For in-depth study of the synthesized films, the microstructural parameters such as crystallite size, strain and dislocation density of $Sn_3Sb_2S_6$ thin films particles are studies by taking the slow scan X-ray diffraction (XRD) pattern around the (416) orientation. The crystallite size (D) of the $Sn_3Sb_2S_6$ films is calculated by using Scherrer's formula [4].

$$D = \frac{k\lambda}{B\cos\theta} \tag{1}$$

where D is the crystallite size in Å, λ is the wavelength of the used X-ray in Å, β is the full width at half maximum (FWHM) of diffraction peak in radians, θ is the
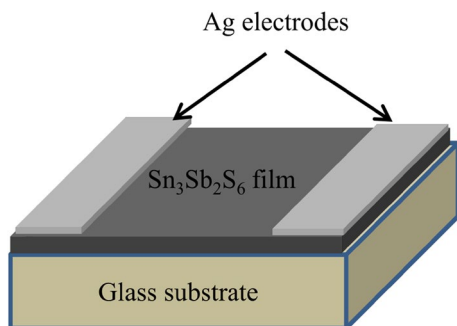
corresponding Bragg angle in degree and K is a constant of approximate 0.9.

The lattice strain (ε) was calculated by using the Scherrer's relation [4].

$$\varepsilon = \frac{\beta}{4\tan\theta} \tag{2}$$

The dislocation density (δ), defined as the length of dislocation lines per unit volume (Å^{-2}) of the crystal, was evaluated from the formula [5]:

$$\delta = \frac{1}{D^2} \tag{3}$$

3 Results and discussion

3.1 XRD and SEM study

Figure 3 presents XRD diffraction patterns of the synthesized thin films. For all diffractograms, the major XRD diffraction peak that appeared at angular position of $2\theta = 31.71°$ is attributed to (416) reflection plane of orthorhombic $Sn_3Sb_2S_6$ phase according to (JCPDS, card no. 38-0826). Minor secondary diffraction lines may be observed at $2\theta = 15.61°$ for glancing angle $\alpha = 0°$ and $2\theta = 39.17°$ for $\alpha = 40°$ witch correspond respectively to (106) and (813) planes of $Sn_3Sb_2S_6$ material. No peak related to impurity was observed; furthermore, the diffraction lines were sharp, which indicate the good crystalline quality and purity of the as obtained $Sn_3Sb_2S_6$ films.

As can be seen from Fig. 3, the peak intensity decreases when deposition angle increases from 0 to 85° and then drops sharply to present only few traces. This behavior can be linked to the shadowing effects and limited adatom
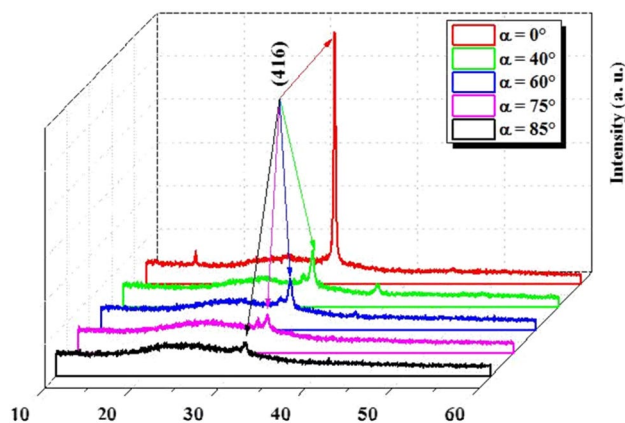

Fig. 2 Sample configuration for electrical measurements

Fig. 3 X-ray diffraction patterns of $Sn_3Sb_2S_6$ thin films deposited at different incident angles

diffusion, which prevents the diffusivity of deposited atoms at room temperature [6].

Therefore, the structural properties of $Sn_3Sb_2S_6$ are affected by the flux incident angle especially for the higher oblique angles. This result is in agreement with that observed for other materials developed under the same conditions [7, 8].

The microstructural parameters D, ε and δ of $Sn_3Sb_2S_6$ thin films are summarized in Table 1.

It can be shown that the crystallite size decreases from 330 to 165 Å with increasing incident angle α. This implies that the increased incident angle will lead to degradation in the crystallinity of the films. In addition, the decrease in the crystallite size indicates an increase in the lattice defects, which in turn grow internal strain and dislocation density (Table 1).

Figure 4 shows the top-view and cross-sectional scanning electron microscopy (SEM) images of $Sn_3Sb_2S_6$ thin films deposited with an incidents angles of α = 0°, 40°, 60°, 75° and 85°.

As can be seen, the microstructure of thin film is formed by homogenously distributed columns, and it was affected by modifying the glancing angle from 0° to 85°. Indeed when increasing the incident angle, the materials exhibit a porous surface and the columns were separated by an accentuated voids. This change may be explained by the shadowing geometry and limited diffusion during film growth [6]. Moreover, greater incident deposition angle produces more voids in the surface and in volume of thin films materials and larger separations between neighboring nanocolumns [9].

Cross section SEM images of the specimens with the different glancing angles (α = 0°, 40°, 60°, 75° and 85°) is shown in Fig. 4. As can be seen, at normal incidence (α = 0°), the film shows a dense and compact structure. However, at α = 40°, 60°, 75° and 85° the SEM micrographs showed a nanocolumnar structure separated by voids. Voids are known to be formed as a consequence of both surface roughness and shadowing effects [10]. Thus, the structure passes from densified columnar structure to a porous columnar one at high incident angle due to the shadowing effect and limited adatom diffusion. This behavior may be used in

several optoelectronic applications such as distributed Bragg reflectors films [11, 12], photonic crystals [13] and rugate filters [14, 15]. Deeper analysis of cross-section micrographs shown in Fig. 4, exhibited systematically a strange phenomenon, i.e. after about 300 nm thick, column angle seems to be changed. This angle is even more accentuated as the glancing angle increases. This behavior may be related to the coupling of both strains and voids effects. By increasing glancing angle, more voids were observed and further growth, induces higher strain on grown columns which may affect their orientation. This behavior was also observed by Parra-Barranco et al. [16] on thin ITO films fabricated by e-beam evaporation technique at oblique angle condition.

3.2 Impedance study

In this item, the conductivity in terms of both temperature and frequency has been carried out to investigate the conducting state in $Sn_3Sb_2S_6$ thin films for different glancing angles (α = 0°, 40°, 60°, 75° and 85°). Typical complex impedance curves of Z″ as a function of Z′ in temperatures range (420–500 °C) are displayed in Fig. 5 for glancing angles α = 0°, 60°, and 85°.

The analysis of experimental data of all samples, show that when temperature increases, the semi-circles are slightly depressed and their maximum shift to higher frequencies. Moreover, the diameter and the maximum of semi-circles decreases with increasing temperature as well as with glancing angle. These observations lead to the conclusion that the electrical conductivity is thermally activated well as the relaxation times distribution [17]. The Cole–Cole plot of impedance at different glancing angle, showed the presence of one semi-circular arc, indicating parallel RC elements originating from the grains. In order to investigate the relaxation time as a function of temperature, we plot Z″ versus frequency at different temperatures Fig. 6.

It is known that Z″ passes through a maximum at $\omega_m\tau = 1$, where τ represents the mean value of the relaxation time distribution. We spotted that the maximum in Z″ peak shifts to higher frequency with the temperature [18]. This phenomenon reveals that the peak frequency indicating Arrhenius behavior and then we can determine the activation energy. The relaxation frequency of these samples obeys to the well-known Arrhenius law [19]:

$$\omega_m = \omega_0 e^{-\frac{Ea}{K_B T}} \qquad (4)$$

where ω_0 is a constant, K_B is the Boltzmann constant in (eV K^{-1}) and E_a is the activation energy in (eV).

In this case, E_a represents the difference between the trap level and the conduction band. Thus and as shown in Fig. 7, the expression of Ln(ω_m) = f(1000/T) leads to a linear function, in good agreement with expression Eq. (4).

Table 1 Structural parameters derived from XRD patterns for $Sn_3Sb_2S_6$ thin films deposited at different incident angles

Incident angle α(°)	Grain size (Å)	δ (×10^{14} m^{-2})	ε (×10^{-2})
0	330	11	21.7
40	277	13	30.9
60	213	22	33.5
75	198	25	36.2
85	165	37	43.8

Fig. 4 Top-view and Cross-sectional SEM images of the $Sn_3Sb_2S_6$ thin films: **a** $\alpha = 0°$, **b** $\alpha = 40°$, **c** $\alpha = 60°$, **d** $\alpha = 75°$, **e** $\alpha = 85°$
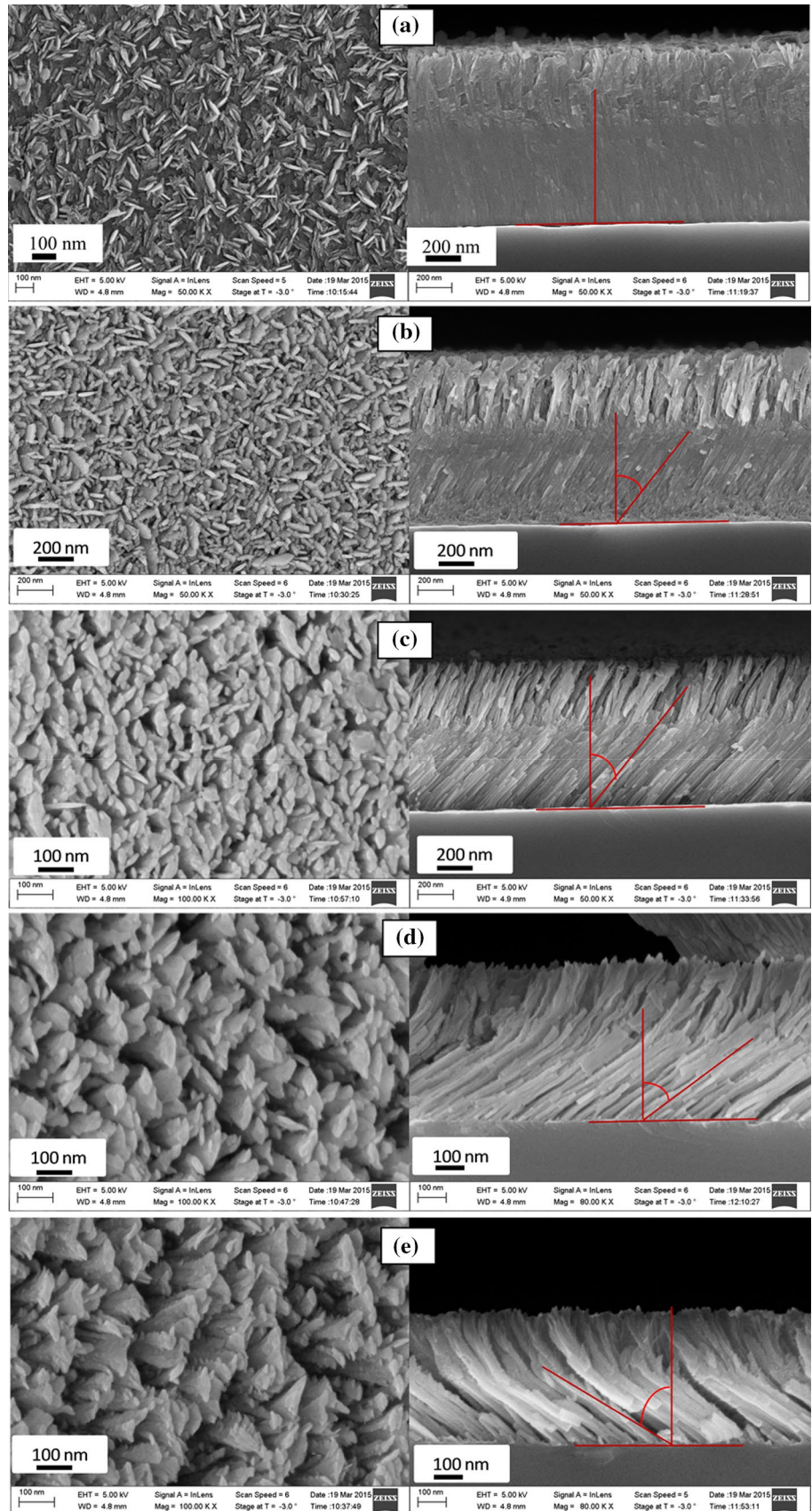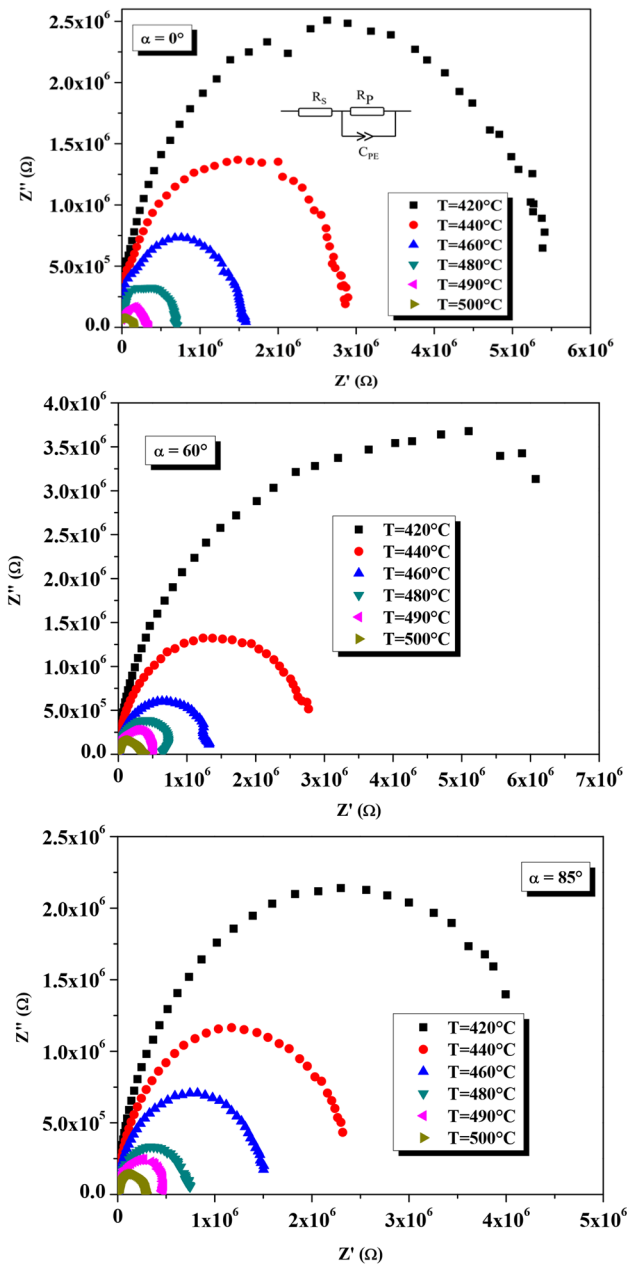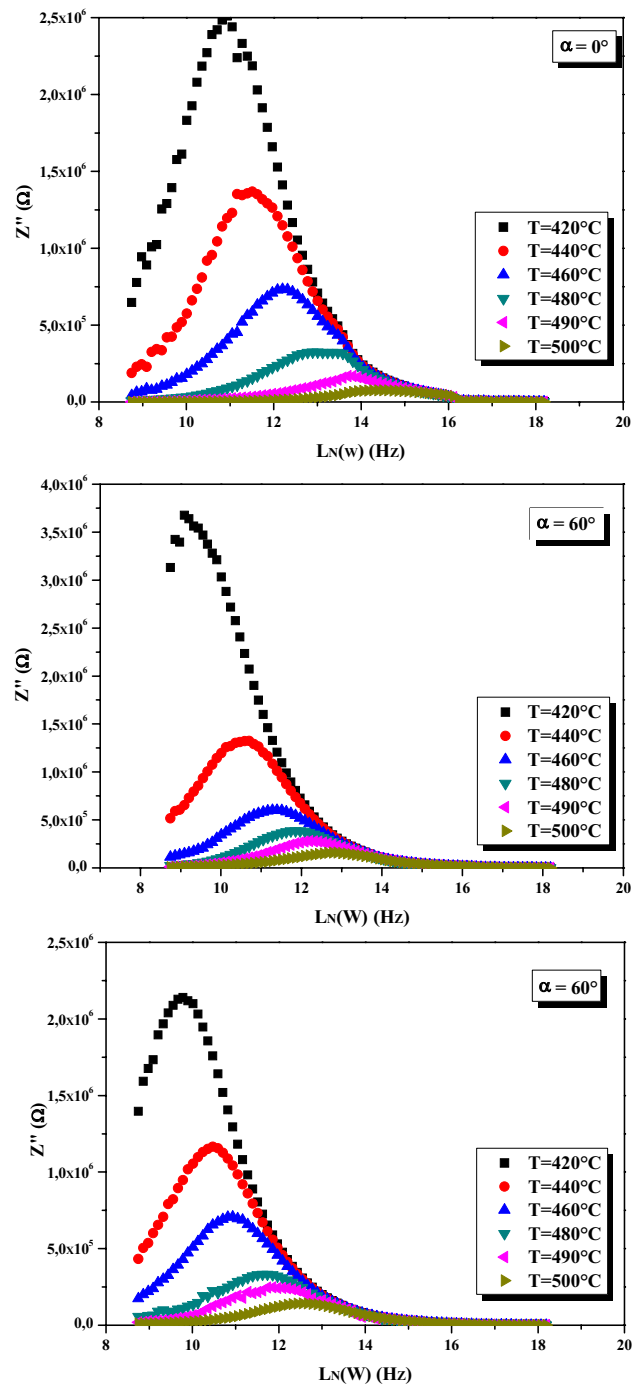
Fig. 5 Complex impedance spectra at various temperatures of $Sn_3Sb_2S_6$ thin films deposited at different flux angle ($\alpha = 0°$, 60° and 85°), inset ($\alpha = 0°$) equivalent circuit diagram

Fig. 6 Frequency dependence of Z'' at different temperatures of $Sn_3Sb_2S_6$ thin films deposited at different flux angles ($\alpha = 0°$, 60° and 85°)

The calculated values of the activation are summarized in Table 2. We note that the calculated values of the activation energy seem to vary softly for glancing angles under 75° and significant decrease may be observed for $\alpha = 85°$.

On the other hand AC conductivity measurements have been broadly used to investigate the nature of defect centers in disordered systems since it is assumed that they are responsible for this type 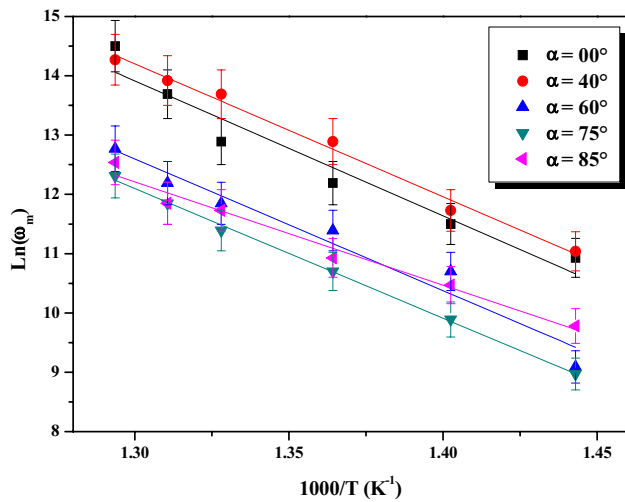of conduction. Figure 8 exhibits the total conductivity (σ_T) as a function of applied frequency and can be written:

$$\sigma_T = \sigma_{DC} + \sigma_{AC} \tag{5}$$

where σ_{DC} and σ_{AC} are respectively the DC and AC conductivities.

Fig. 7 Temperature dependence of angular frequency relaxation of $Sn_3Sb_2S_6$ thin films for different glancing angles

Table 2 Calculated values of activation energy E_a

Incident angle α (°)	$E_{a(Z'')}$ (meV)	$E_{a(DC)}$ (meV)
0	195	199
40	192	197
60	191	163
75	188	153
85	149	147

The AC conductivity is related by a simple expression given by Jonscher's power law [20]:

$$\sigma_{AC} = A\omega^S \tag{6}$$

where A is a pre-exponential constant, $\omega = 2\pi f$ is the angular frequency and s is the power law exponent where $0 < s < 1$.

At low angular frequency; σ_T has a small variation with frequency then it increases with increasing frequency.

which is calculated by extrapolation of the curves of σ_t to zero frequency for different temperatures. In the higher frequency domain, conductivity increases linearly with frequency. This frequency behavior in this type of materials is proportional to ω^s ($s \leq 1$). Figure 8 shows the typical plot of $Ln(\sigma_T)$ versus $Ln(\omega)$ at various temperatures for thin films synthesized at $\alpha = 0°$, $60°$ and $85°$.

In the higher frequency domain, conductivity increases linearly with frequency for all samples, while at low frequencies it is almost independent on frequency, which could be assigned to DC contribution. It is found that AC conductivity shifts to higher frequency with the temperature, which agrees with the observed shift of the relaxation frequency. The result leads to the conclusion that the observed shift originated from a thermally activated process.
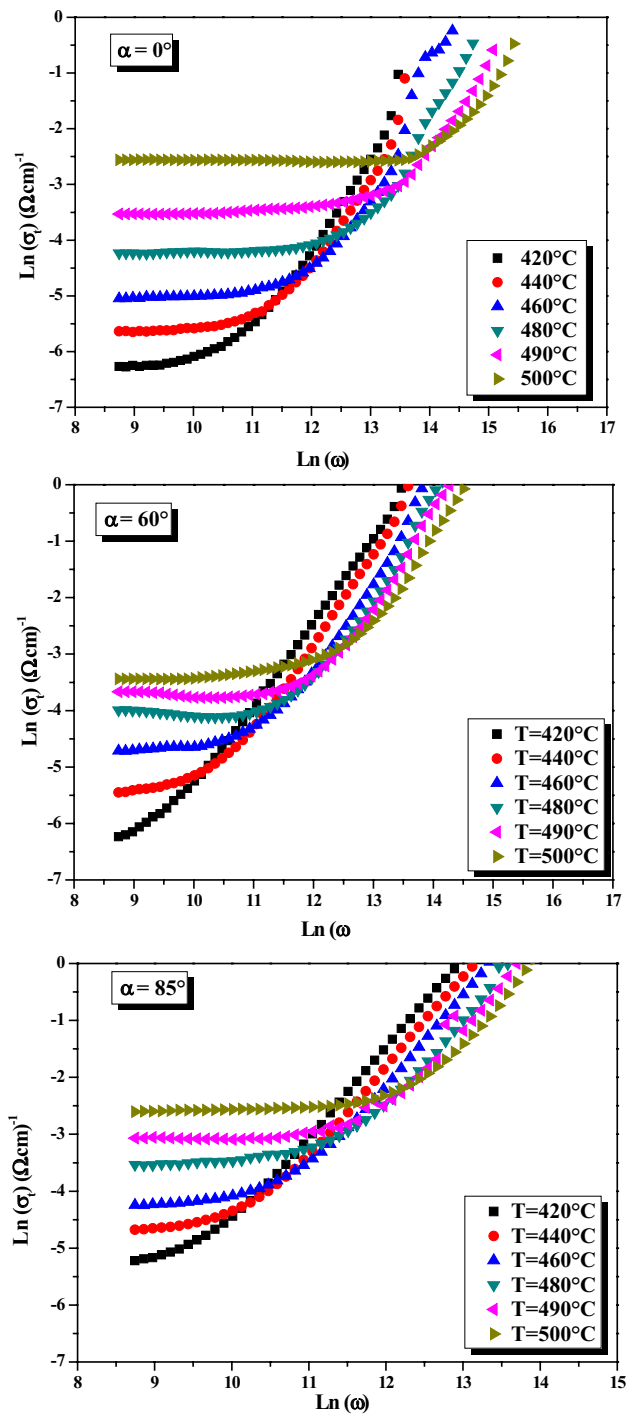
Fig. 8 Angular frequency dependence of σ_T conductivity at different temperatures

Furthermore, this conductivity dependence on frequency is an indication of hopping conduction at higher frequency between localized states [21]. The high-frequency dependence of the AC conductivity may be observed in varieties of semiconductors and can be
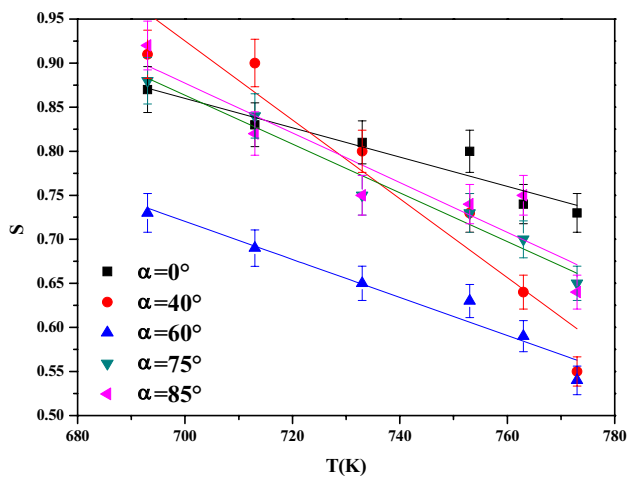
Fig. 9 Temperature dependence of the angular frequency exponents

Fig. 10 Plot of Ln (σ_{DC}) versus 1000/T

explained by hopping of charge carriers between localized sites over the potential barrier [19].

The study of the temperature dependence on the angular frequency exponent s can be used to validate if the hopping pattern is consistent with the correlated barrier hopping (CBH) model [18]. The variation of angular frequency exponent s as a function of temperature for different samples is shown in Fig. 9. It is clear from this figure that, s decreases with increasing temperature.

The variation of DC conductivity with the reciprocal temperature for these films is investigated in order to identify the origin of the conduction process. The experimental data of the DC conductivity is analyzed using the following formula:

$$\sigma_{DC} = Ae^{-\frac{Ea}{K_B T}} \tag{7}$$

where E_a is the activation energy for the hopping conduction in (eV), K_B is the Boltzmann constant in (eV K^{-1}), T the measurement temperature in (K) and A is a constant in $(\Omega\ m)^{-1}$.

Figure 10 shows the variation of DC conductivity as Ln(σ_{DC}) with the reciprocal of the temperature for all samples.

The activation energy, $E_{a(DC)}$ is determined from the slope of Ln(σ_{DC}) versus 1000/T. The obtained values of $E_{a(DC)}$ are summarized in Table 2 and they are in consistent with the value deduced from the relaxation frequency ($E_{a(Z'')}$). This confirms that it is the same conduction mechanism where localized charge carriers are involved in both transport phenomena. Indeed, the perusal of experimental data suggests that the DC conductivity is thermally activated hopping of localized charge carriers in the band gap.
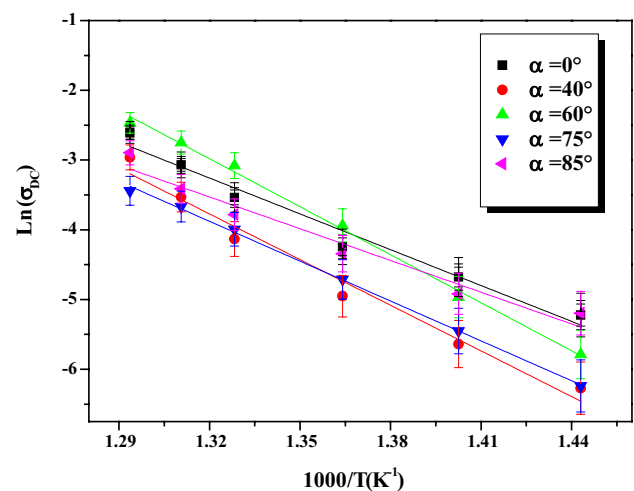
4 Conclusion

In summary, we have studied the effect of GLAD technique on structural, morphological and electrical behaviors of $Sn_3Sb_2S_6$ thin films prepared by single source vacuum thermal evaporation method. XRD results show that the crystallinity of the film disproves as the incident angle increases. SEM micrographs of the GLAD $Sn_3Sb_2S_6$ films show a highly oriented microstructure composed of slanted columns and separated by voids. The advantages of possible control and easy monitoring of material porosity, makes the GLAD technique very promising for optical and optoelectronic device applications such as the distributed Bragg reflectors films, photonic crystals and rugate filters. Using impedance spectroscopy technique, the electrical microstructures of the $Sn_3Sb_2S_6$ thin films were investigated. This method offers an approaching and easy way to explain the phenomena of the conduction mechanism within the thin film materials. In conclusion this study allowed us to understand some aspects of the electrical behavior of the new high absorbent $Sn_3Sb_2S_6$ semiconductor material.

References

1. A. Larbi, H. Dahman, M. Kanzari, Effect of substrate temperature on structural and optical properties of the new high absorbent $Sn_3Sb_2S_6$ thin films. Vacuum **110**, 34–39 (2014)
2. P.P.K. Smith, Structure determination of diantimony tritin hexasulphide $Sn_3Sb_2S_6$ by high-resolution transmission electron microscopy. Acta Crystallogr. C **40**, 58–584 (1984)
3. A. Barranco, A. Borras, R. Agustin, A. Gonzalez-Elipe, Palmero, Perspectives on oblique angle deposition of thin films: from fundamentals to devices. Prog. Mater. Sci. **76**, 59–153 (2016)

4. B.D. Cullity, *Elements of X-ray Diffraction*. (Addison-Welsley, London, 1978)

5. G.B. Williamson, R.C. Smallman, Dislocation densities in some annealed and cold-worked metals from measurements on the X-ray Debye-Scherrer spectrum. Philos. Mag. **1**, 34–45 (1956)

6. A. Harizi, A. Sinaoui, F. Chaffar Akkari, M. Kanzari, Physical properties of $Sn_4Sb_6S_{13}$ thin films prepared by glancing angle deposition method. Mater. Sci. Semicond. Process. **41**, 450–456 (2016)

7. A. Sinaoui, F. Chaffar Akkari, B. Gallas, M. Kanzari, Comparative study of structural and morphological properties of nanostructured $CuIn2n + 1S3n + 2(n = 0,1$ and 2) thin films produced by oblique angle deposition. Eur. Phys. J. Appl. Phys. **64**, 20301(1)–20301(8) (2013)

8. A. Sinaoui, F. Chaffar Akkari, B. Gallas, D. Demaille, M. Kanzari, Ellipsometric characterization and optical anisotrpy of nanostructured $CuIn_3S_5$ and $CuIn_5S_8$ thin films. Thin Solid Films **590**, 111–117 (2015)

9. S. Wang, G. Xia, H. Hea, K. Yia, J. Shao, Z. Fan, Structural and optical properties of nanostructured TiO_2 thin films fabricated by glancing angle deposition. J. Alloy. Compd. **431**, 287–291 (2007)

10. A.R. Shetty, A. Karimi, M. Cantoni, Effect of deposition angle on the structure and properties of pulsed-DC magnetron sputtered TiAlN thin films. Thin Solid Films **519**, 4262–4270 (2011)

11. J.W. Leem, J.S. Yu, Broadband, and wide-angle distributed Bragg reflectors based on amorphous germanium films by glancing angle deposition. Opt. Express **20**, 20576–20581 (2012)

12. J.W. Leem, J.S. Yu, Glancing angle deposited ITO films for efficiency enhancement of a-Si:H/μc-Si:H tandem thin film solar cells. Opt. Express **19**, 258–269 (2011)

13. S.J. Jang, Y.M. Song, C.I. Yeo, C.Y. Park, Y.T. Lee, Highly tolerant a-Si distributed Bragg reflector fabricated by oblique angle deposition. Opt. Mater. Express **1**, 451–457 (2011)

14. J.J. Steele, M.J. Brett, Nanostructure engineering in porous columnar thin films: recent advances. J. Mater. Sci.: Mater. Electron. **18**, 367–379 (2007)

15. K. Kaminska, T. Brown, G. Beydaghyan, K. Robbie, Circular birefringence dependence on chiral film porosity. Appl. Opt. **42**, 4212–4219 (2003)

16. J. Parra-Barranco, F.J. García-García, V. Rico, A. Borra, C. López-Santos, F. Frutos, A. Barranco, A.R. González-Elipe, Anisotropic in-plane conductivity and dichroic gold plasmon resonance in plasma-assisted ITO thin films e-beam-evaporated at oblique angles. ACS Appl. Mater. Interfaces **7**, 10993–11001 (2015)

17. I. Trabelsi, N. Ben Mehrez, M. Kanzari, Electrical characterization of $SnSb_4S_7$ thin films by impedance spectroscopy. J. Mater. Sci.: Mater. Electron. **26**, 7763–7770 (2015)

18. A. Mhamdi, B. Ouni, A. Amlouk, K. Boubaker, M. Amlouk, Study of nickel doping effects on structural, electrical and optical properties of sprayed ZnO semiconductor layers. J. Alloy. Compd. **582**, 810–822 (2014)

19. T. Nagata, T. Shimura, A. Ashida, N. Fujimura, T. Ito, Electro-optic property of ZnO:X(X = Li,Mg) thin films. J. Cryst. Growth **237**, 533–537 (2002)

20. A.K. Jonscher, The 'universal' dielectric response. Nature **267**, 673–679 (1976)

21. R. Ondo-Ndong, G. Ferblantier, F. Pascal-Delannoy, A. Boyer, A. Foucaran, Electrical properties of zinc oxide sputtered thin films. Microelectron. J. **34**, 1087–1092 (2003)